ETH zürich

ETH Library

Design principles of operando ultraviolet-visible and electron paramagnetic resonance spectroscopy setups for active site characterization in ion-exchanged zeolites

Journal Article

Author(s):
Fischer, Jörg Wolfram Anselm; Buttignol, Filippo; Brenig, Andreas; Klose, Daniel; Ferri, Davide; Sushkevich, Vitaly; van Bokhoven, Jeroen Anton; Jeschke, Gunnar

Publication date:
2024-03-01

Permanent link:
https://doi.org/10.3929/ethz-b-000657569

Rights / license:
Creative Commons Attribution 4.0 International

Originally published in:
Catalysis Today 429, https://doi.org/10.1016/j.cattod.2023.114503

Funding acknowledgement:
ETH-48 20-1 - Time-resolved in situ EPR spectroscopy for heterogeneous catalysis (ETHZ)

This page was generated automatically upon download from the ETH Zurich Research Collection.
For more information, please consult the Terms of use.

Catalysis Today 429 (2024) 114503

Contents lists available at ScienceDirect

Catalysis Today

journal homepage: www.elsevier.com/locate/cattod

Design principles of *operando* ultraviolet-visible and electron paramagnetic resonance spectroscopy setups for active site characterization in ion-exchanged zeolites

Jörg Wolfram Anselm Fischer [a,1], Filippo Buttignol [b,1], Andreas Brenig [c,d,1], Daniel Klose [a], Davide Ferri [b,*], Vitaly Sushkevich [d,*], Jeroen Anton van Bokhoven [c,d,**], Gunnar Jeschke [a,*]

[a] Institute of Molecular Physical Science, ETH Zurich, Vladimir-Prelog-Weg 1-5/10, CH-8093 Zurich, Switzerland
[b] Paul Scherrer Institute, Forschungsstrasse 111, CH-5232 Villigen, Switzerland
[c] Institute for Chemical and Bioengineering, ETH Zurich, Vladimir-Prelog-Weg 1-5/10, CH-8093 Zurich, Switzerland
[d] Laboratory for Catalysis and Sustainable Chemistry, Paul Scherrer Institute, Forschungsstrasse 111, CH-5232 Villigen, Switzerland

ARTICLE INFO

Keywords:
Heterogeneous catalysis
Zeolites
Operando spectroscopy
Electron paramagnetic resonance spectroscopy
UV-Visible spectroscopy
Modulated excitation spectroscopy

ABSTRACT

Cu- and Fe-exchanged zeolites have been widely investigated for their applicability in selective partial oxidation of CH_4 and abatement of environmentally harmful nitrogen oxides. However, the differentiation between spectator and active sites is cumbersome due to their dynamic co-existence, which aggravates the elucidation of the redox dynamics of the latter. Therefore, correlated multi-spectroscopic approaches carried out under *operando* conditions are needed in order to disentangle the inherent reactivity of specific species. Here we describe the conceptualization of complementary operando spectroscopic methods for the investigation of ion-exchanged zeolites employed in redox reactions. The potential and versatility of this approach are demonstrated by means of two exemplary case studies. First, we present the insight generated by two custom operando ultraviolet-visible and electron paramagnetic resonance spectroscopy setups operating in batch mode into CH_4-to-CH_3OH conversion over Cu-exchanged mordenite. In addition to recording the method-dependent spectroscopic fingerprints of distinct Cu centers, the overall CH_4 consumption is simultaneously monitored in both setups. The extracted apparent activation energies of the reactive centers obtained from the two systems are in good agreement with each other allowing to link the bulk reactivity to the intrinsic site-specific kinetics of all Cu centers. Second, the EPR setup is equipped with a flow reactor designed to carry out modulated excitation experiments with phase-sensitive detection in order to improve the signal-to-noise ratio and time resolution. The cell is employed to study the conversion of NO via selective catalytic reduction over Fe-exchanged ferrierite. In combination with *operando* X-ray absorption spectroscopy, a small portion of active Fe species consisting of monomers in gamma-positions and oligomeric structures located in the main channel is identified, which are kept in a redox active state under relevant reaction conditions and thus sustain the chemical transformation of NO.

1. Introduction

Redox-mediated reactions are fundamental processes in the field of heterogeneous catalysis in which the chemical transformation of single or multiple reactants to products is coupled with a reversible change in the valence state of one or more redox centers [1,2]. In this view, zeolites have attracted enormous scientific attention in the last decades for their ability to accommodate extra-framework ions (e.g., Cu and Fe), which can undergo such a reversible change in the oxidation state [3]. However, an in-depth molecular understanding of these redox active sites is hindered by the heterogeneous Cu and Fe speciation often characterizing these materials and the lack of site-selective spectroscopic tools.

Ultraviolet-visible (UV-Vis) and electron paramagnetic resonance

* Corresponding authors.
** Corresponding author at: Institute for Chemical and Bioengineering, ETH Zurich, Vladimir-Prelog-Weg 1-5/10, CH-8093 Zurich, Switzerland.
E-mail addresses: davide.ferri@psi.ch (D. Ferri), vitaly.sushkevich@psi.ch (V. Sushkevich), jeroen.vanbokhoven@chem.ethz.ch (J.A. van Bokhoven), gunnar.jeschke@phys.chem.ethz.ch (G. Jeschke).
[1] These authors have contributed equally.

https://doi.org/10.1016/j.cattod.2023.114503
Received 19 October 2023; Received in revised form 21 December 2023; Accepted 27 December 2023
Available online 28 December 2023
0920-5861/© 2023 The Author(s). Published by Elsevier B.V. This is an open access article under the CC BY license (http://creativecommons.org/licenses/by/4.0/).

(EPR) spectroscopy are valuable techniques for studying heterogeneous catalysts on a fundamental level by providing information about distinct catalytic functionalities via detection of their method-specific spectroscopic fingerprints [4]. Such a detailed atomistic insight into the structure, environment, and electronic state of the active sites as well as potential reaction intermediates under controlled conditions (in situ) is imperative to gain a deeper understanding of the mechanistic functioning of the catalyst [4–7].

Considering that both spectroscopic techniques are characterized by specific capabilities, limitations, and requirements, their combination yields a more comprehensive picture of the catalytic system [4,8]. This is further emphasized by the fact that heterogeneous catalysts may simultaneously host a variety of different active sites as well as inactive spectator species depending on their composition, structure, and morphology [7–9]. One particularly suitable example, which demonstrates the complementary information provided by both UV-Vis and EPR spectroscopy is the identification and characterization of the various Cu^{2+} sites present in Cu-exchanged zeolites [3,10,11]. For instance, UV-Vis spectra of Cu-exchanged mordenite (Cu-MOR) exhibit an absorption feature at ~13600 cm^{-1} after high temperature treatment in O_2/He, which has been attributed to a d-d transition of bare Cu^{2+} ions located in close proximity to two framework Al tetrahedral sites (T-sites) [12]. Nevertheless, a distinction between Cu^{2+} centers placed into environments characterized by different Al T-site arrangements is not feasible by UV-Vis spectroscopy, since the low symmetry, structural variability, and energetic similarity of the possible cation exchange sites results in broad and overlapping signals [13]. On the contrary, the $g_{||}$ splitting region in the X-band EPR spectra of dehydrated Cu-MOR is more sensitive towards the exact location of the Al T-sites and two features characterized by $g_{||}$ values of 2.331 and 2.326 have been observed [14,15]. These signals have been associated to bare Cu^{2+} ions situated in the vicinity of either a -AlOSiOAl- or a -$AlO(SiO)_2$Al- sequence revealing that two different types of Cu^{2+} ions in distinct environments give rise to the absorption band at ~13600 cm^{-1}.

However, the unambiguous identification of individual Cu^{2+} species in Cu-exchanged zeolites by EPR spectroscopy is limited to materials with a low Cu^{2+} content since EPR spectra are subjected to severe line broadening at higher Cu-loadings due to more pronounced magnetic dipolar interactions [13,16]. Additionally, a higher Cu^{2+} content may lead to the creation of EPR-silent species as a result of an antiferromagnetic coupling of the unpaired electrons in adjacent or bridged Cu^{2+} centers [17]. This limitation is particularly troublesome considering that multimeric Cu^{2+} moieties containing bridging extra-framework O-ligands have been identified as the active sites in partial CH_4 oxidation and NO/N_2O decomposition [10,18–21]. As opposed to EPR spectroscopy, these Cu-Oxo species can be readily identified by UV-Vis spectroscopy on the basis of their characteristic $O_{bridge} \rightarrow Cu^{2+}$ ligand-to-metal charge transfer (LMCT) transitions [22]. The highly distinct sensitivity of UV-Vis and EPR spectroscopy towards agglomerated and isolated Cu^{2+} species, respectively, has been exploited by Sushkevich *et al.* [23] and Fischer *et al.* [24] in order to study the behavior of dimeric and combined monomeric Cu^{2+} active sites in selective CH_4 oxidation. The kinetic properties of $[Cu_2(\mu\text{-}O)]^{2+}$ centers as well as Cu^{2+} and $[CuOH]^+$ ions have been extracted by monitoring the temporal evolution of the corresponding method-specific spectroscopic fingerprints revealing that dimeric Cu^{2+} active sites exhibit a faster reaction rate and higher apparent activation energy than combined monomeric species.

Although UV-Vis spectroscopy enables a qualitative assessment of the presence of multimeric Cu-Oxo moieties, it does not straightforwardly provide quantitative information, since the molar absorption coefficients of these agglomerated Cu^{2+} centers are not known. Furthermore, UV-Vis studies of Cu-exchanged zeolites need to be conducted in diffuse reflectance mode meaning that the beam penetration depth and scattering coefficient have to be constant in order to ensure a linear correlation between specimen concentration and absorbance [13,25,26]. On the contrary, the content of paramagnetic Cu^{2+} sites can be determined directly by EPR spectroscopy by comparing the normalized integral intensity of the spectrum of a reference material with known spin concentration to the one of the sample spectrum assuming comparable material properties and instrument settings [27]. Using aqueous Cu^{2+} reference solutions, it has been shown that the amount of Cu^{2+} in hydrated Cu-zeolites measured under ambient conditions corresponds to the total Cu^{2+} concentration as determined by elemental analysis [28,29]. Considering that the hydrated state is the initial stage in every experiment, this correlation enables the quantification of EPR-active Cu^{2+} species at every other moment later on e.g. after dehydration/activation [15]. Comparing the concentration of EPR-active Cu^{2+} after treatment in O_2 to the total Cu^{2+} content has, furthermore, been used by Bruzzese *et al.* [30] to indirectly determine the amount of EPR-silent Cu^{2+} species such as multimeric centers.

In addition to the study of Cu-exchanged zeolites, coupled UV-Vis/EPR spectroscopic approaches have also been successfully employed in the characterization of other heterogeneous catalysts [31–33]. Brückner, for example, combined UV-Vis, EPR, and Raman spectroscopy as well as an on-line gas chromatograph (GC) in a single reactor setup to assess the structure and valence state of the VO_x active sites in V/TiO_2 catalysts during C_3H_8 dehydrogenation [33]. The work by Brückner can be considered as an example for the application of UV-Vis and EPR spectroscopy in the *operando* mode, since the spectroscopic characterization is accompanied by the simultaneous measurement of the catalytic reactivity under realistic working conditions [32]. Considering that heterogeneous catalysts undergo dynamic adsorbate-induced structural transformations even upon slightly changing the chemical environment, only *operando* experiments enable a direct correlation of the catalytic reactivity to the behavior of the observed spectroscopic fingerprints [6,34]. This understanding, in turn, is an indispensable requirement for a more rational design of catalytically active materials with precisely tailored reactivity, selectivity, and stability [4,34].

Therefore, *operando* methodologies still require further development in order to improve time-resolution, signal-to-noise ratio (SNR), and site specificity [4,7,35]. Increasing the speed of spectra acquisition by e.g. pump-probe spectroscopy while maintaining a decent SNR allows to monitor the dynamic transformations of the catalyst in real-time and facilitates the detection of short-lived intermediates [7,34,36]. Additionally, the collection of large spectroscopic datasets enables the extraction of pure spectral components and intensity profiles via chemometric methods, whereby the latter can be used to determine site-specific kinetic information and activation energies [5,7,20]. Furthermore, enhancing site specificity by e.g. coupling complementary spectroscopic techniques or performing modulated excitation with phase sensitive detection (ME-PSD) experiments can simplify the differentiation of active sites from spectator species [4,35–38].

In this contribution, we describe the design of complementary *operando* UV-Vis and EPR batch setups and demonstrate their utilization in the case study of CH_4-to-CH_3OH conversion over Cu-MOR. Owing to the method-specific capabilities of the two techniques, the spectroscopic fingerprints of different Cu species situated in distinct framework positions and characterized by a discrete coordination geometry and nuclearity can be observed. More precisely, *operando* UV-Vis spectroscopy allowed to study the behavior of dimeric Cu-Oxo centers, whereas *operando* EPR was used to follow the development of monomeric Cu sites during the reaction. In this process in the absence of oxygen, the reaction product remains adsorbed to the zeolite. Therefore, instead of assessing the material reactivity via detection of desorbed reaction products, the CH_4 partial pressure was recorded in both setups during spectra acquisition, which is equivalent to monitoring the reactant consumption [11,23,24]. The evolution of the individual spectroscopic signals as well as the system pressure were used to extract the kinetic properties and activation energies of the distinct Cu active sites revealing a high degree of conformity between the two setups. Additionally, the EPR setup was complemented with a flow reaction cell and with a separated

experimental setup equipped with fast switching valves allowing ME-PSD experiments. This setup was used to investigate the reversible redox dynamics of active Fe species in a commercial Fe-ferrierite (Fe-FER) catalyst during the conversion of NO via selective catalytic reduction (SCR) by perturbing the system with repeated pulses of O_2. By combining the results with *operando* X-ray absorption near edge structure (XANES) experiments, various distinct Fe species characterized by specific redox transitions were identified.

2. Material and methods

2.1. Sample preparation and physicochemical characterization

Partial CH_4 oxidation reactions were conducted using a previously prepared Cu-MOR material with a Cu-loading of 5.16 wt% and a silicon-to-aluminum (Si/Al) ratio of 6.5. Further details about the synthetic procedure as well as the physicochemical properties are described elsewhere [24].

The Fe-FER catalyst for the NO-SCR study was a commercial material (CASALE SA) characterized by a Fe loading of 0.7 wt% and a Si/Al ratio of 9.4. A full characterization of the sample can be found elsewhere [39].

2.2. Pretreatment and activation of Cu-MOR

The typical pretreatment consists of a dehydration step at 723 K in vacuum for at least 4 h, a calcination step at 723 K in ~400 mbar pure O_2 for 4 h, and a second dehydration step at 723 K in vacuum for 4 h. Since the reactions were carried out in a subsequent manner, the initial dehydration step was performed only once in the beginning. The activation was performed at 723 K in ~400 mbar pure O_2 for 1 h followed by a final dehydration step at 623 K in vacuum for 1 h. In order to prevent excessive autoreduction, the cooling step between the activation and the final dehydration was conducted in an O_2 atmosphere. An overview of the methods and used materials can be found in Table 1.

2.3. Operando UV-Vis spectroscopy

Operando UV-Vis experiments were carried out in a home-built reactor setup consisting of a vacuum rig, a gas supply system, a temperature-controlled quartz cell, a light source, a spectrometer, and a reflection probe. The vacuum rig and gas supply system are installed into an open rack frame. The vacuum rig is composed of an Edwards E2M 1.5 dual stage rotary vane pump (final pressure: 1.5×10^{-3} mbar), a Pfeiffer Vacuum MVP 015–2 diaphragm pump (final pressure: 3.5 mbar), and an air-cooled Pfeiffer Vacuum HiPace 80 turbomolecular pump (final pressure: $<5 \times 10^{-10}$ mbar). The setup can be operated between ~5×10^{-7} and 1000 mbar, effectively. The rotary vane pump is linked to a cooling trap (150 mL condensate capacity, 1000 mL coolant capacity), which is connected to the gas supply system via a spherical ground joint retainable by a spring-loaded metal clip. The diaphragm pump acts as a booster pump for the turbomolecular pump. The latter is controlled by a Pfeiffer Vacuum DCU 110 display control unit and is connected to the gas supply system via an angle valve. A Pfeiffer Vacuum ActiveLine Transmitter PKR 251 (pressure range: 5×10^{-9} – 1000 mbar), which is connected to a Pfeiffer Vacuum SingleGauge TPG 261, is installed in front of the angle valve.

The gas supply system (depicted in Scheme 1) is a borosilicate glass line (Willi Möller) exhibiting seven ports in total, two of which are connected to the cooling trap and the turbomolecular pump. A Pfeiffer Vacuum ActiveLine Transmitter CMR 363 (pressure range: 1×10^{-3} – 11 mbar) and a Pfeiffer Vacuum ActiveLine Transmitter CMR 361 (pressure range: 0.1–1100 mbar) controlled by a Pfeiffer Vacuum TPG 366 MaxiGauge are mounted to two other ports. Two further ports enable flexible and controllable gas feeding. The remaining port is connected to the temperature-controlled quartz cell (illustrated in Scheme 2) via a borosilicate linkage. The total volume of the gas supply system and the quartz cell amounts to ~570 mL. To evaluate the leak rate of the system, the pressure increase of the evacuated system during a time period of ~2 days at room temperature has been measured (Fig. S1, Table S1).

The quartz cell is a unilaterally sealed cylindrical case, which is connected to a fixation rod to mitigate movement of the cell throughout the measurement. Typically, a square Cu-MOR sample pellet with a mass of approximately 150 mg is inserted into the cell and positioned above a reference white standard (parent Na-MOR zeolite). Subsequently, the cell is installed into an insulating fumed silica block. Heating and temperature control are achieved by a heating cable and a thermocouple connected to a Lumel RE92 dual loop controller. A six-around-one (six illumination and one read fiber, 400 μm) Avantes reflection probe (wavelength range: 200–2500 nm), which is mounted to a height-adjustable clamp, is directed onto the quartz cell through a slit in the alumina block. The fibers are coated with a metal cladding and the tip of the probe is gas-cooled, allowing measurements at temperatures up to 1073 K. The illumination fibers are connected to an Ocean Optics DH-2000-BAL deuterium/halogen lamp (wavelength range: 210–2500 nm), whereas the read fiber is attached to an Ocean Optics Maya 2000-Pro spectrometer (wavelength range: 165–1100 nm) equipped with a 2D charge-coupled device (CCD) area image sensor.

After pretreating and activating the Cu-MOR sample, ~9.5 mbar CH_4 (Messer, grade: 4.5) were introduced into the setup at temperatures ranging from 473 to 513 K while UV-Vis spectra and the system pressure were simultaneously recorded. Usually, 125 spectra were averaged, the spectrometer integration time was set to 80 ms, and a delay time of 20 s was imposed resulting in a total time resolution of 30 s. A boxcar smoothing with a window width of five to seven points was applied. Difference spectra were calculated by subtracting the reflectance spectra recorded throughout the reaction from the initial reflectance spectrum of the freshly activated material.

Table 1
Overview of the measurement parameters.

Setup	Material	Measurement of catalytic activity	Temperature range	Temporal resolution	Identified species	Sample mass
UV-Vis (batch)	Cu-MOR[a]	Educt consumption via pressure drop in the reactor cell	473–513 K	30 s	Dimeric species in Cu-MOR	150 mg
EPR (batch)	Cu-MOR[a]	Educt consumption via pressure drop in the reactor cell	473–513 K	34 s[c]	Monomeric species in Cu-MOR	30 mg
EPR (flow trough)	Fe-FER[b]	Mass spectrometer at the exhaust at the cell	673 K	58 s[c]	Monomeric Fe species and Fe_xO_y species	15 mg
XAS	Fe-FER[b]	Mass spectrometer at the exhaust at the cell	673 K	0.5 s	All Fe species without site specificity	40 mg

[a] The Cu-MOR was dehydrated in a vacuum at 723 K before an activation at 723 K in pure O_2.
[b] The Fe-FER was dehydrated in Ar at 673 K followed by equilibration in 1000 ppm NO-NH_3/Ar.
[c] Note, that the time resolution of the EPR is not only limited by the sweep time (see Table S2-S3), but also by the time the electromagnet needs to stabilize the field after each scan. This "dead time" is taken into account in the time reported here.

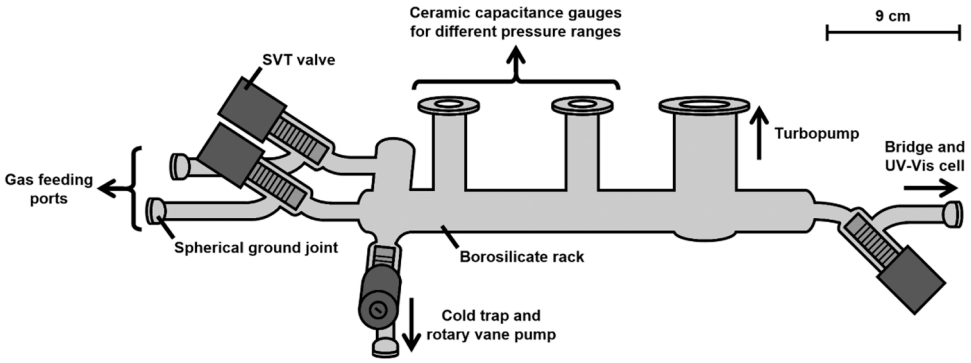

Scheme 1. Gas supply system of the *operando* UV-Vis setup operating in batch mode.

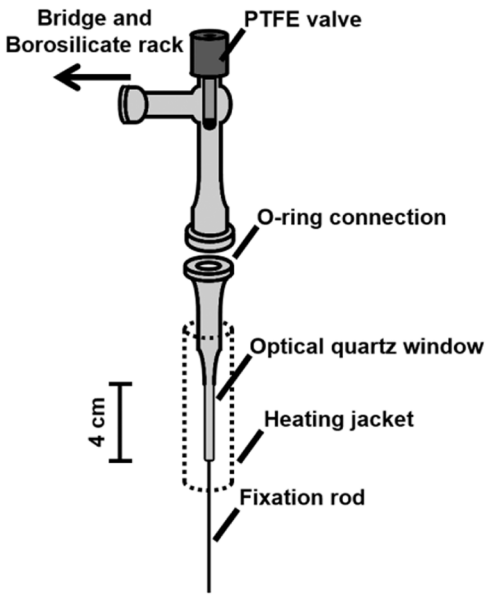

Scheme 2. Temperature-controlled quartz cell of the *operando* UV-Vis setup.

2.4. *Operando* EPR spectroscopy

Operando EPR spectroscopy experiments were performed using a homebuilt water-cooled high-temperature resonator, which was installed into a continuous-wave (cw) EPR spectrometer (Bruker EMX) operating at X-band frequencies (~9.265 GHz) [40]. The resonator is heated by a flow of hot N_2 using a home-built temperature controller. Two different gas supply systems were used, depending on whether the reaction was carried out in batch or in flow-through configuration.

The batch reactor setup (shown in Scheme 3) is comprised of 1/8″ Swagelok tubing and has two connections equipped with Swagelok two-way valves leading to CH_4 and O_2 gas lines, respectively. Two high-precision pressure gauges (Pfeiffer) for the pressure ranges from 1 – 11 and 10 – 1000 mbar are connected via KF-16 flanges using Alu edge type seals. The gas dosing and pressure measurement part is separated from the turbomolecular pump and the EPR reactor by two Swagelok two-way valves. A needle valve is employed to enable a controlled evacuation of the system by the turbomolecular pump, since no secondary pump was installed. Swagelok stainless steel flexible vacuum bellows, connected to the Swagelok tubing via a KF-16 flange using an Alu edge type seal, bridge the adapter of the EPR reactor with the gas supply system. The adapter (depicted in Scheme 4a) is connected to the stainless steel bellows via another flange using an NW aluminum centering ring and comprises of a stainless steel hollow cylinder. It can be stabilized with a holder from the back removing any tension from the quartz-based EPR reactor. The latter is attached to the holder via a plug-in connection comprised of two rubber o-rings. The total volume of the setup including the EPR reactor is about 27 mL ensuring a high sensitivity towards measuring pressure changes. The setup can be operated between 1×10^{-7} and 1000 mbar. The setup has been tested for leakages by measuring the pressure increase of the evacuated system during a time period of ~2 days at room temperature (Fig. S1, Table S1).

For the CH_4-to-CH_3OH batch experiments carried out using Cu-MOR, around 30 mg of the sieved material (250–500 μm) was inserted into the quartz EPR reactor (Wilmad; 4 mm OD) and fixated with a quartz wool plug. The material was subjected to the pretreatment and activation protocol and subsequently exposed to ~9.5 mbar CH_4 (Messer, grade 4.5). In situ experiments were performed at room temperature before and after the dosage of CH_4. *Operando* experiments were carried out by monitoring the system pressure and changes in the EPR spectrum simultaneously throughout the reaction at temperatures ranging from 473 to 513 K. The evolution of the EPR signals was evaluated by means of the intensity of the double integral of the baseline corrected cw spectra. A spectrum prior to the dosage of CH_4 was used as an experimental baseline. The intensity of the cw EPR spectrum is proportionally related to the first derivative of the magnetic susceptibility of the sample at a certain temperature and external magnetic field strength.

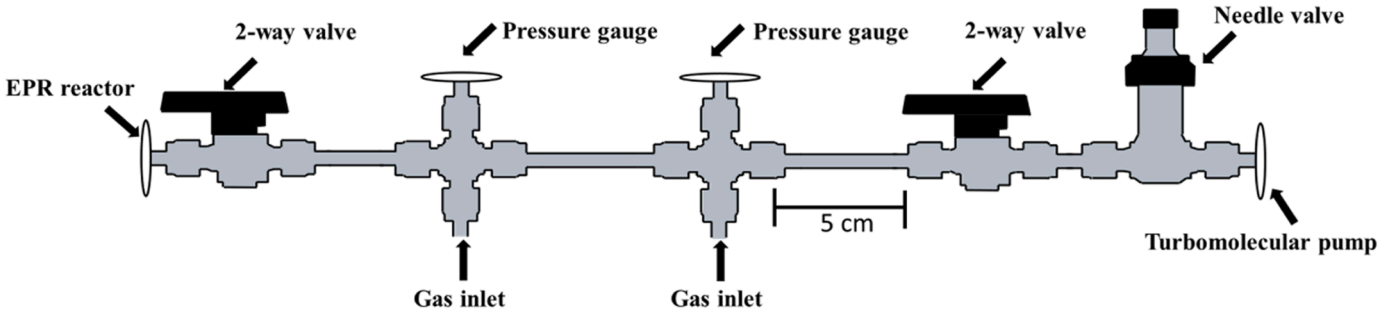

Scheme 3. Gas supply system of the *operando* X-band EPR setup operating in batch mode.

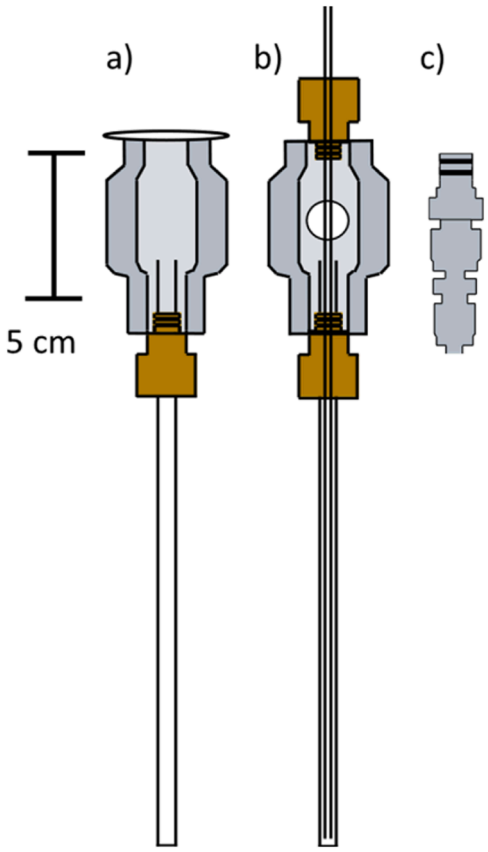

Scheme 4. Adapters for the *operando* EPR setups: (a) For the batch setup configuration, (b) for the flow through setup, (c) connections for the flow though setup.

Accordingly, the double integral of the EPR spectrum is a direct measure of the total number of spins in the sample. The standard procedure to determine the concentration is double integration of the spectrum [27]. The measurement parameters for in situ and *operando* experiments for the batch reactor study can be found in Table S2.

For the NO-SCR flow-through experiments, 1/16″ Swagelok tubing ensured flexibility and minimized the dead volume. The flow-through cell consisted of a thin capillary (Qsil: 2.0–2.4 mm OD) inserted inside the EPR quartz reactor (Wilmad; 4 mm OD) used for the batch experiments (Scheme 4b). This assembly was connected to the gas supply system via the hollow adapter shown in Scheme 4c. The catalyst bed (ca. 15 mg of 100–150 μm Fe-FER) was fixed between two quartz wool plugs in the inner capillary to ensure maximal contact with the reaction gas mixture. The experimental setup consisted of mass flow controllers (Bronkhorst) and solenoid valves (Series 9, Parker) to control the gas flows and automatically switch between gases, respectively. A total flow rate of 15 mL•min^{-1} was used for the in situ EPR and *operando* ME experiments.

In situ experiments were performed by equilibrating Fe-FER at 673 K in a flow of i) Ar, ii) 3 vol % O_2/Ar iii) 1000 ppm NO + 1000 ppm NH_3/Ar or iv) 1000 ppm NO + 1000 ppm NH_3 + 3 vol % O_2/Ar. After steps i) and ii) the sample was cooled down in the same atmospheres and EPR spectra were measured at 323 K.

ME experiments were performed by pulsing 3 vol % O_2/Ar over Fe-FER equilibrated at 673 K in a constant flow of 1000 ppm NO + 1000 ppm NH_3/Ar. Thirty pulses were performed while recording a total of 20 spectra (1 spectrum = 59.8 s) in one full period (two consecutive pulses each of 598 s). The measurement parameters for in situ and ME flow through EPR experiments are reported in Table S3. In order to construct the time-domain concentration profile for the Fe_γ^{3+} site, line shape simulations were performed that approximate the signal centred at $g = 4.3$ with a Voigt profile (see Fig. S11).

2.5. Operando XANES

Operando XANES experiments were performed at the SuperXAS beamline of the Swiss Light Source (SLS; Villigen, Switzerland). A silicon-coated mirror was used to collimate the X-ray polychromatic beam originating from a 2.9 T bending magnet. Monochromatic light was obtained through a channel cut Si(311) liquid N_2 cooled monochromator, which also allowed collection in quick-scanning extended X-ray absorption fine-structure spectroscopy (QEXAFS) mode at 1 Hz [41]. The X-ray beam (1 × 0.2 mm) was successively filtered using a 40 μm Al filter in order to avoid possible undesired phenomena such as hot-spots [42] and X-ray induced reduction of Fe centers [43]. Measurements were performed in fluorescence mode at the Fe K-edge (7.112 keV) using a passivated implanted planar silicon (PIPS) detector [44]. Around 40 mg of sieved catalyst were loaded into a custom-made spectroscopic cell designed for XANES measurements [45]. Two quartz wool plugs were used to fix the catalyst bed between two graphite windows (0.5 mm thick). A K-type thermocouple inserted in the spectroscopic cell (ca. 1 mm aside the catalyst bed) was used to monitor and control the reaction temperature. A total flow rate of 50 mL•min^{-1} was used for pre-treatment and the ME experiment. Fe-FER was pre-treated in 3 vol % O_2/Ar at 673 K for 30 min and successively equilibrated in 1000 ppm NO + 1000 ppm NH_3/Ar at the same temperature. The ME experiment was later performed by pulsing 3 vol % O_2/Ar over Fe-FER equilibrated at 673 K in a constant flow of 1000 ppm NO + 1000 ppm NH_3/Ar. Pulses were performed every 120 s for 2 h while recording a total of 480 spectra in one full period (1 spectrum = 0.5 s). For absolute energy calibration, the stainless steel body of the custom-made spectroscopic cell was measured for 20 s before focusing the beam onto the catalyst bed. The raw XANES spectra were processed, calibrated and normalized using a Python-based processing software for QEXAFS data [46].

A Pfeiffer Vacuum OmniStar MS connected downstream of the cell was used for on-line monitoring of the outlet gas concentrations by following fragments with a mass-to-charge ratio (m/z) of 17 (NH_3), 18 (H_2O), 28 (N_2), 30 (NO), 32 (O_2), 40 (Ar). In order to account for possible fluctuations in the total flow rate, the ion currents of each fragment were normalized by the one of Ar after each experiment.

3. Results

3.1. Operando UV-Vis and EPR spectroscopy of Cu-MOR during partial CH_4 oxidation

UV-Vis and EPR spectroscopy have been employed to determine the Cu speciation and the site specific kinetics of dimeric and monomeric centers in Cu-MOR, respectively. In analogy to Fischer *et al.*, Cu-MOR has been activated and subsequently exposed to ~9.5 mbar CH_4 and the evolution of the spectra have been recorded in combination with the CH_4 pressure [24]. The corresponding in situ spectra before and after the reaction are shown in Fig. 1. The in situ UV-Vis spectrum (Fig. 1a) of activated Cu-MOR exhibits absorption bands (local minima in reflectance) at ~12,900 cm^{-1}, 26,800 and 35,800 cm^{-1}. The former feature has been attributed to a d-d transition in bare Cu^{2+} ions with an open d-electron shell ($3d^9$), which are placed into the crystal/ligand field of the surrounding zeolite matrix [10,12,42,47,48]. The two latter signals originate from LMCT transitions [3,11,47]. The band at about 26,800 cm^{-1} has been associated with an LMCT transition involving extra-framework O-ligands and Cu^{2+} in dimeric $[Cu_2(\mu\text{-}O)]^{2+}$ centers, whereas the feature at ~35,800 cm^{-1} arises from LMCT transitions between framework O-atoms and Cu^{2+} [11,23,24,47]. Upon contacting the activated Cu-MOR with CH_4, the absorbance of these signals decreases indicating the consumption of the dimeric Cu-Oxo species as well as a change in the coordination to the lattice [23,24]. On the contrary, an

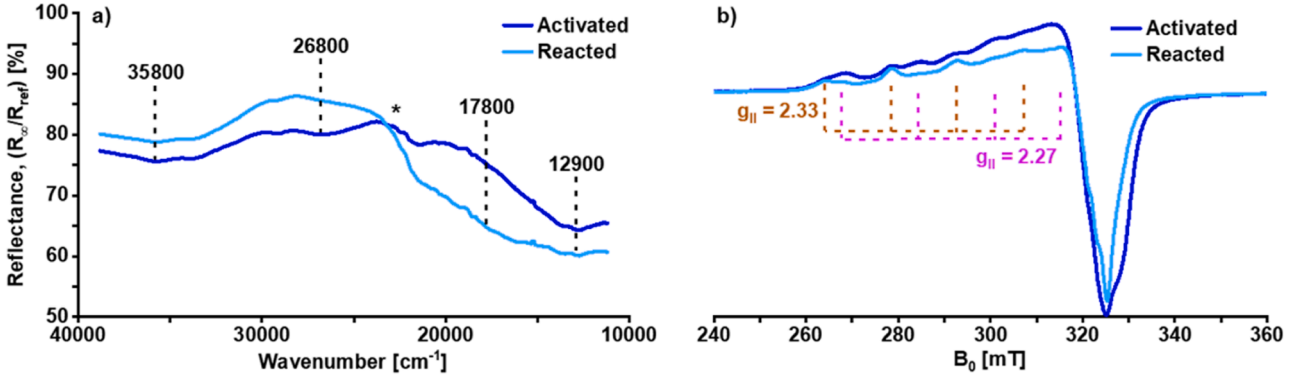

Fig. 1. (a) In situ UV-Vis spectra of activated (blue) and reacted (light blue) Cu-MOR at 473 K. (b) In situ EPR spectra of activated (blue) and reacted (light blue) Cu-MOR at room temperature.

increased absorbance at about 17,800 cm^{-1} can be observed, which has been associated to the adsorption of reaction products, whose precise nature has not been identified so far [23]. The hyperfine splitting in the $g_{||}$ region arising from the interaction of the Cu^{2+} nucleus (I = 3/2) with its unpaired electron ($3d^9$ electronic configuration) is highly sensitive towards the Cu coordination environment causing the in situ EPR spectrum of activated Cu-MOR to exhibit two distinct species (Fig. 1b) [12,23]. One Cu site is centered around $g_{||} = 2.27$ and has been attributed to a $[CuOH]^+$ center, whereas the second species, which has been assigned to a bare Cu^{2+} ion is characterized by $g_{||} = 2.33$ [49,50]. The spectrum is severely broadened due to Cu – Cu dipolar interactions preventing the detection of further species, as has been reported in a previous study on this material [24]. The reduction of Cu^{2+} results in a closed shell d^{10} configuration, causing Cu^+ to be EPR silent. Hence, the signal intensity of Cu centers involved in the redox cycle decreases throughout the exposure to CH_4. As it can be seen in Fig. 1b, the signal intensity of all present Cu^{2+} species is reduced after reaction with CH_4, indicating that both $[CuOH]^+$ and bare Cu^{2+} ions are able to participate in the redox process. Note, that the amount of reduced bare Cu^{2+} is considerably lower compared to $[CuOH]^+$. This is a direct consequence of their different reactivity toward CH_4 [12,23,24,51,52]. In addition to the signal reduction, the spectrum of reacted Cu-MOR becomes narrower due to the weakening of the Cu – Cu interaction. Kinetic analysis of the *operando* UV-Vis and EPR data (Fig. S2 – S4, Table S4 – S6) yield the activation energies of both dimeric and monomeric species, respectively, which are in full agreement with our previously published results using the same material [24].

During the reaction, the consumption of CH_4 can be monitored by recording the pressure in both systems. Since formed reaction products including CH_3OH/CH_3O (selectivity > 90 %) and a small fraction of overoxidation products remain adsorbed on the material at the chosen reaction temperature, the decay is governed solely by the CH_4 consumption [23,24]. The logarithmic plots of the pressure drop are shown in Fig. 2 and reveal two distinct kinetic regimes. As shown previously, these two different kinetic regimes can be attributed to the different active sites in the Cu-MOR material [23,24]. The fast decay at the beginning is governed by the reaction of dimeric $[Cu_2(\mu\text{-}O)]^{2+}$ species, whereas the slower segment originates from the reactivity of the $Cu^{2+}/[CuOH]^+$ monomeric sites. The total CH_4 loss can, therefore, be described as a sum of two first-order reaction rate equations where each first-order reaction rate term accounts for the conversion of CH_4 by either dimeric or monomeric active sites, respectively (Fig. S3, Table S7 – S9, Scheme S1, Eq. S1). Considering the excess of dosed CH_4 with respect to the amount of Cu within the sample and the low CH_4 conversion, which is below 10 %, the reaction was assumed to be pseudo zero-order towards CH_4. On the basis of the deduced reaction rate constants for either dimeric or monomeric active centers, the activation energies can be determined. The resulting Arrhenius plots are shown in Fig. 2, validating the correlation of the UV-Vis and EPR results by showing the same activation energies for both setups. The obtained results are in excellent agreement with our previously reported values on the same material [24].

3.2. *ME-PSD applied to operando XANES and EPR spectroscopies over Fe-FER during NO-SCR*

In addition to the batch reactor employed in the to the study on the CH_4-to-CH_3OH oxidation over Cu-MOR, we implemented a flow-through reactor cell for EPR spectroscopy to investigate the SCR of NO over a commercial Fe-FER catalyst. *Operando* X-ray absorption near edge

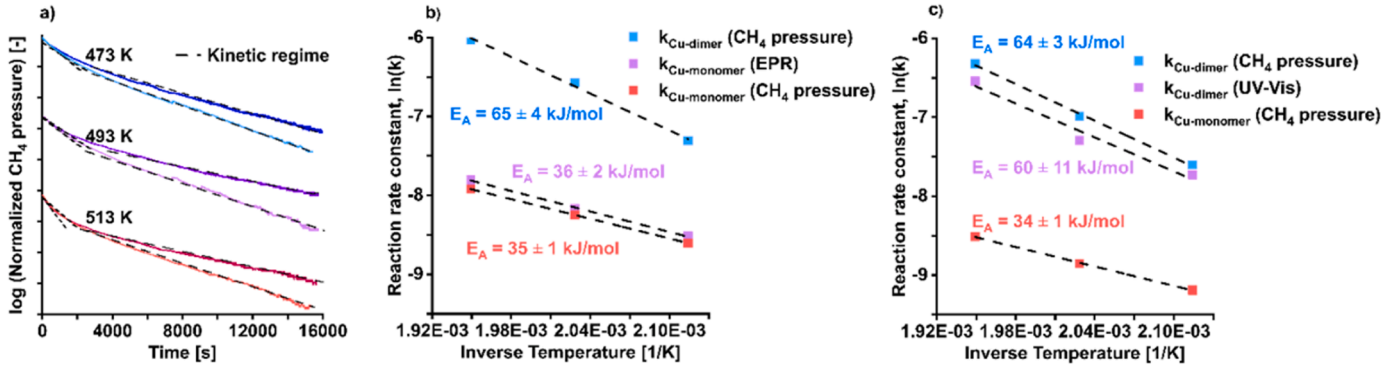

Fig. 2. Logarithmic plots of the pressure decay in the *operando* UV-Vis (dark) and *operando* EPR (pale) setup at 473 K, 493 K and 513 K (a). Arrhenius plots of dimeric and monomeric Cu active sites on the basis of the reaction rate constants obtained from either UV-Vis spectroscopy or the recorded CH_4 pressure (b) Arrhenius plots of dimeric and monomeric Cu active sites on the basis of the reaction rate constants obtained from either EPR spectroscopy or the recorded CH_4 pressure (c).

structure (XANES) spectroscopy was first employed as a state-of-the-art spectroscopic tool for the investigation of redox processes (Fig. 3). Fe-FER was equilibrated under a continuous flow of NO + NH_3, and successively perturbed by O_2 pulses in order to turn the reaction on/off in an alternating fashion according to the ME approach [37]. The time-domain XANES spectra (Fig. 3a) show only a minor shift of the absorption edge towards higher energies in O_2-rich conditions, indicative of a higher average valence state adopted by some Fe atoms [53]. Upon application of PSD analysis (Fig. 3b), additional subtle variations are captured with high SNR in both the pre-edge region (7112 and 7115 eV) and along the absorption edge (7122 and 7125 eV). In the former case, the two contributions are assigned to 1 s → 3d electronic transitions in Fe cations possessing the +2 and +3 oxidation state, respectively [54]. Their anti-phase behavior suggests that the content of Fe^{2+} decreases whereas the one of Fe^{3+} increases in the presence of O_2. This is in agreement with the loss of intensity in the spectral features located around 7122/7125 eV, assigned to 1s → 4p transitions in Fe^{2+} cations [55,56]. Simultaneously, the on-line MS (Fig. S6) indicated the consumption of NO and production of N_2 and H_2O during the O_2-rich part of the pulse sequence, thus demonstrating effective chemical transformation of the feed via NO-SCR under this set of experimental conditions.

In order to complement the information provided by XAS, *operando* EPR spectroscopy was employed to identify the Fe species present in this Fe-FER catalyst and to obtain site-selective insights into their possible redox dynamics. Due to their half-integer spin state, only Fe^{3+} sites are EPR-accessible under our experimental conditions, whereas the integer-spin Fe^{2+} and Fe^{4+} cations remain EPR-silent [3]. Comparison between the spectra recorded in Ar and 3 vol % O_2/Ar at 673 K (Fig. S7) revealed an increase in the intensity of three spectral features, thus suggesting that three different Fe^{3+} sites are created upon oxidation from their corresponding Fe^{2+} state. The broad signal resonating at $g' = 2$ likely corresponds to a combination of Fe-oxide clusters possessing different nuclearity ($Fe^{3+}_{cluster}$) according to the temperature dependence of this transition [57]. The signal at $g' = 4.3$ corresponds to isolated high-spin Fe^{3+} sites in a tetrahedral coordination, based on the large rhombicity (E = D/3) of the zero-field splitting, and are accommodated in the γ position (Fe^{3+}_{γ}), a complex framework structure composed of 5-membered rings in the FER cavity [58,59]. Finally, species exhibiting signals at $g' = 6$ are assigned to isolated high-spin Fe^{3+} sites in the beta (β) position (Fe^{3+}_{β}) [60,61]. Similar to Fe^{3+}_{γ}, Fe^{3+}_{β} sites are also located in the FER cavity but are characterized by an on-plane coordination in the distorted 6-membered ring. [54] Accordingly, Fe-FER possesses a complex heterogeneous Fe speciation, in agreement with the conclusions derived from complementary characterization tools [39].

Upon equilibration in 1000 ppm NO + 1000 ppm NH_3/Ar at 673 K and by comparison with the spectra of the O_2-treated catalyst, a pronounced loss of intensity is observed in the whole spectral range (Fig. S8). This observation is especially true for the Fe^{3+}_{β} sites, whose intensity is completely lost. Introduction of 3 vol % O_2 and equilibration under NO-SCR conditions do not induce changes in the Fe^{3+}_{β} sites, and only a slight increase in intensity of the signals associated to Fe^{3+}_{γ} and $Fe^{3+}_{cluster}$ can be observed. However, given the low SNR and the small extent of these variations it is challenging to determine the effective development of any transitions between these sites. In order to enhance the SNR while retaining sufficient time-resolution, we conducted *operando* ME experiments (Fig. 3c,d, Fig. S9) using the same set of experimental conditions employed in the XANES experiments. In agreement, the on-line MS (Fig. S10) indicated occurrence of the NO-SCR reaction during the O_2 pulses. Due to the ME approach, the time-resolved EPR spectra (Fig. 3c) are now characterized by a superior SNR and a clear increase in intensity is observed in the transitions associated with Fe^{3+}_{γ} and $Fe^{3+}_{cluster}$ in the O_2-rich part of the pulse sequence. Additionally, analysis of the phase-resolved data (Fig. 3d) indicates that these sites undergo continuous and reversible changes in signal intensity during the whole experiment. The intensity decreases upon O_2 cut-off and re-increases once O_2 is introduced. On the contrary, the signal attributed to Fe^{3+}_{β} sites does not contribute to the demodulated spectra, probably because the intensity associated with their transition remain negligible also in the time-domain.

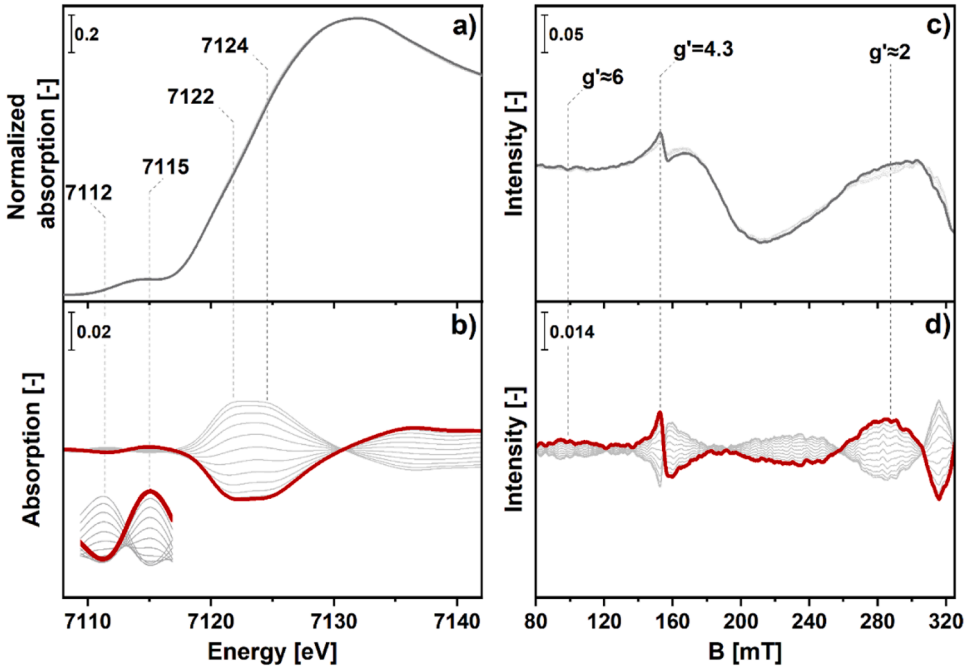

Fig. 3. (a, c) Averaged time-resolved and (b, d) corresponding phase-resolved *operando* (a,b) XANES and (c, d) EPR spectra of Fe-FER during (a, b) 2-min and (c, d) 10-min pulses of 3 vol % O_2/Ar in a constant flow of 1000 ppm NO and 1000 ppm NH_3/Ar at 673 K. The inset in (b) is a magnification of the pre-edge region. The colored spectra in (b) and (d) are drawn to guide the eye.

4. Discussion

The design of two *operando* UV-Vis and EPR batch setups has been described and their performance has been benchmarked and compared in partial CH_4 oxidation, using a previously characterized Cu-MOR sample with a Cu loading of 5.16 w % [21,22]. Instead of assessing the material productivity via on-line detection of desorbed reaction products, the CH_4 pressure is measured in both setups, which is equivalent to monitoring the reactant consumption.

In agreement with our earlier findings, UV-Vis and EPR spectroscopy indicate the presence of at least three different Cu species, including $[Cu_2(\mu\text{-}O)]^{2+}$ sites (26,800 cm^{-1}), $[CuOH]^+$ centers ($g_{||} = 2.27$), and bare Cu^{2+} ions ($g_{||} = 2.33$), which are active in partial CH_4 oxidation [21,22]. As opposed to UV-Vis spectroscopy, dimeric Cu-Oxo moieties are not detectable via EPR spectroscopy as a result of the antiferromagnetic coupling of the O-bridged Cu^{2+} ions [10]. On the contrary, $[CuOH]^+$ species, which have been reported to exhibit a d-d feature at 16,750 cm^{-1}, were not detected by UV-Vis spectroscopy due to the overlap with the strong d-d signal of bare Cu^{2+} ions at ~12900 cm^{-1} [12]. Their identification is further aggravated by the intrinsic broadness of absorption bands of condensed matter in UV-Vis spectroscopy induced by the blurring from rovibrational transitions and spin-orbit coupling [27,33]. Therefore, the combination of UV-Vis and EPR spectroscopy provides complementary results by probing the method- and site-specific spectroscopic fingerprints of distinct Cu^{2+} centers yielding a more complete understanding of the speciation in the Cu-MOR material.

By tracing the development of the spectroscopic fingerprints of dimeric and monomeric Cu^{2+} active sites in the UV-Vis and EPR setups, respectively, their activation energies have been determined. The obtained kinetic properties have been correlated to the overall material activity deduced from the loss in CH_4 pressure. This approach enables the prediction of the reaction rates of active centers, which cannot be detected by the individual techniques alone. As shown in Fig. S3 and S5, the activation energies of the dimeric and combined monomeric Cu^{2+} active sites obtained from the *operando* UV-Vis and EPR setups are in high agreement with each other demonstrating that both systems yield complementary and comparable data. These results are in line with our earlier study on the same material [24]. The kinetic properties of the individual Cu^{2+} species enable a full description of the total CH_4 consumption during the experiments highlighting the descriptive power of correlated spectroscopic techniques conducted in appropriately designed reaction cells.

A comparison between the logarithmic rates of the pressure decay (Fig. 2) indicates that the reaction rates of $[Cu_2(\mu\text{-}O)]^{2+}$ moieties obtained from the *operando* UV-Vis setup are on average slower by a factor of 0.95 than in the EPR system. Moreover, the average ratio of the logarithmic rates of $Cu^{2+}/[CuOH]^+$ species between the *operando* UV-Vis and EPR setup amounts to 0.93. These variations can be explained by the uncertainties and local gradients in temperature within both systems as well as the differences in sample packing considering the utilization of a pressed pellet in UV-Vis measurement and a lose powder in EPR experiments. This is an intrinsic limitation of working with two different spectroscopic setups, which has to be accepted due to the necessity of measuring a white reference prior to the UV-Vis experiments.

The design of the flow-through cell has been described and the suitability has been demonstrated by monitoring the NO-SCR reaction and by correlation of the recorded data with operando XANES data obtained under the same conditions. The phase-resolved XANES spectra indicated that a fraction of Fe^{2+} cations undergo reversible Fe^{2+}/Fe^{3+} redox transitions during O_2 pulses (Fig. 3). The simultaneous occurrence of the NO-SCR reaction (Fig. S6) suggests that the reduction of NO by NH_3 requires this reversible dynamic redox behavior. However, since the majority of the XANES signal appears to be static during the ME experiments (Fig. 3a), just a minor fraction of the total Fe^{2+} atoms in Fe-FER is being reversibly perturbed by O_2 and thus effectively participates in the redox mediated transformation of the feed. This is in agreement with the small changes in the time-resolved EPR spectra recorded during introduction of O_2 to the NO-NH_3 equilibrated Fe-FER (Fig. 3c). Given the nature of XANES it is very challenging to derive molecular understanding of the Fe^{2+} species participating in the reaction [62]. Based on the in situ EPR experiments (Fig. S7), a mixture of monomeric Fe species located in different framework positions and coordination environments (Fe_β and Fe_γ) as well as small Fe-oxide agglomerates ($Fe_{cluster}$) can be identified in Fe-FER.

In the presence of NO and NH_3 (Fig. S8) the intensity decreases in the whole EPR spectrum, suggesting that the majority of the Fe sites adopt an EPR-silent Fe^{2+} state irrespective of their framework position and agglomeration degree. However, upon perturbation by repeated O_2 pulses, an increase in intensity in the signals associated to Fe_γ and $Fe_{cluster}$ can be observed (Fig. 3c), indicating that these sites can be reversibly oxidized to EPR-active Fe^{3+}. In addition, these species are also continuously perturbed (Fig. 3d) and are thus kept in a redox active state under these conditions. Therefore, and differently from XANES, EPR spectroscopy allowed to disentangle the contribution of the different Fe sites and to follow their individual redox dynamics during NO-SCR. The low magnitude of the perturbations in the EPR spectra agrees well with the small changes observed in the phase-resolved XANES spectra, likely indicating that the Fe^{2+} to Fe^{3+} transitions in Fe_γ and $Fe_{cluster}$ (Fig. 3d) are responsible for the weak oxidation observed in O_2-rich conditions (Fig. 3b). However, since all Fe_β species, most of the Fe_γ sites, and a part of the $Fe_{cluster}$ remain fully reduced also under NO-SCR conditions, most of the XANES spectrum of Fe-FER is static during the reaction (Fig. 3a). Nevertheless, the small fraction of reactive Fe_γ and $Fe_{cluster}$ sites detected by operando EPR (Fig. 3c) sustain the reversible redox dynamics observed by *operando* XANES (Fig. 3d) and likely ensure chemical transformation of the feed via NO-SCR [63]. In agreement with these conclusions, the redox dynamics monitored via the two spectroscopic tools is similar and follows the transient addition and cut-off of O_2 in the reaction environment (Fig. S11). To get a more detailed kinetic information, the signal of Fe_γ has been simulated with a Voigt profile to enhance the signal-to-noise ratio. As can be seen, the oxidation and the reduction of the iron follows the addition and the removal of O_2 sharply.

The in situ and *operando* EPR experiments also revealed that the Fe_β sites are completely reduced under NO-SCR relevant reaction conditions (Fig. S8 and Fig. 3c). Thus, despite the fact that O_2 can promote $Fe_\beta^{2+}/Fe_\beta^{3+}$ oxidation in Ar (Fig. S8), this re-oxidation step is inhibited in the presence of NO and NH_3. As a result, Fe_β sites do not participate in the reversible redox transformations because they are restrained in a fully reduced state and thus are not active for NO-SCR under these reaction conditions. These conclusions agree with the general accepted knowledge establishing active site/s re-oxidation as the rate-limiting step in NO-SCR over Fe-exchanged zeolites [64]. Furthermore, our results provide unambiguous evidences that different Fe sites are kept in a redox active state and thus are active under high-temperature NO-SCR. These comprise monomeric tetrahedrally-coordinated Fe_γ sites in the FER cavity and also a distribution of larger agglomerated Fe species probably located in the main channels of FER. Finally, it should be noted that despite being redox active, a large fraction of Fe_γ sites remain reduced under our experimental condition and thus, they likely do not participate in the reaction. Uncovering the reasons for this behavior is important to gain a molecular understanding of the NO-SCR reaction over Fe-exchanged zeolites and to further optimize these catalysts for NO conversion applications.

5. Conclusion

The design and performance of custom-made *operando* UV-Vis and EPR setups has been outlined and their capabilities have been assessed in different exemplary redox reactions involving two types of TMI-exchanged zeolites.

In the case of CH_4-to-CH_3OH oxidation using Cu-MOR, both techniques yield complementary information about the Cu speciation of the

sample via the detection of method-specific spectroscopic fingerprints. Based on the recorded changes of these spectroscopic features throughout CH_4 oxidation, the activation energies of both dimeric and monomeric Cu^{2+} active sites have been determined and the obtained values are in good agreement with our earlier study [24]. Additionally, the loss in CH_4 partial pressure, which is caused by the consumption of CH_4 by all present Cu^{2+} active centers, has been measured in both setups to analyze the total kinetics of reactant conversion. It can be shown that the spectroscopically obtained site-specific kinetic properties can effectively be correlated to the overall performance of the material and that the deduced activation energies from both setups are in good agreement with each other.

Furthermore, the *operando* EPR setup has been equipped with a newly designed flow-through reactor cell suitable for ME experiments and its capabilities have been tested for in situ and *operando* studies of a commercial Fe-FER catalyst during NO conversion through SCR reaction. Combining *operando* XANES experiments, we demonstrated that these spectroscopic methods yield comparable results and both indicate that a reversible redox process is involved in the transformation of NO. Nevertheless, while XANES does not allow to differentiate between different iron sites by its nature, EPR spectroscopy allows to disentangle the possible redox transitions in different Fe species under reaction conditions and thus provides active site/s specificity. Accordingly, the results indicate that NO reduction is catalyzed by a minority of isolated Fe site in γ-cationic position and by agglomerates possibly located in the main channels of FER. Differently, monomeric Fe cations in β-cationic position remain largely reduced under reaction conditions and do not exhibit the reversible red-ox dynamic required for the chemical transformation of the feed.

CRediT authorship contribution statement

Andreas Brenig: Data curation, Formal analysis, Investigation, Visualization, Writing – original draft. **Jörg Wolfram Anselm Fischer:** Data curation, Formal analysis, Investigation, Methodology, Visualization, Writing – original draft. **Filippo Buttignol:** Data curation, Formal analysis, Investigation, Visualization, Writing – original draft. **Gunnar Jeschke:** Conceptualization, Funding acquisition, Project administration, Resources, Supervision, Writing – review & editing. **Vitaly Sushkevich:** Conceptualization, Project administration, Supervision, Writing – review & editing. **Jeroen Anton van Bokhoven:** Conceptualization, Funding acquisition, Project administration, Resources, Supervision, Writing – review & editing. **Daniel Klose:** Conceptualization, Writing – review & editing. **Davide Ferri:** Conceptualization, Funding acquisition, Project administration, Resources, Supervision, Writing – review & editing.

Declaration of Competing Interest

The authors declare the following financial interests/personal relationships which may be considered as potential competing interests: Gunnar Jeschke reports that financial support was provided by Swiss National Science Foundation. This work was co-funded by CASALE SA. The other authors declare that they have no known competing financial interests or personal relationships that could have appeared to influence the work reported in this paper.

Data availability

Data will be made available on request.

Acknowledgments

This work was supported by the ETH Zurich [ETH-48 20-1] and the Energy System Integration (ESI) platform of the Paul Scherrer Institute (PSI). The investigation of the NO-SCR reaction was co-founded by the Paul Scherrer Institut (PSI) and we are thankful to the Paul Scherrer Institut (PSI) for beamtime allocation at the SuperXANES beamline (SLS). We gratefully acknowledge the support from René Tschaggelar and Oliver Oberhänsli in the development of the *operando* EPR setup.

Data Availability

Data will be made available on request.

Appendix A. Supporting information

Supplementary data associated with this article can be found in the online version at doi:10.1016/j.cattod.2023.114503.

References

[1] C. Vogt, B.M. Weckhuysen, Nat. Rev. Chem. 6 (2022) 89–111.
[2] R. Schlögl, Angew. Chem. Int. Ed. 54 (2015) 3465–3520.
[3] B.E.R. Snyder, M.L. Bols, R.A. Schoonheydt, B.F. Sels, E.I. Solomon, Chem. Rev. 118 (2018) 2718–2768.
[4] B.M. Weckhuysen, Chem. Soc. Rev. 39 (2010) 4557–4559.
[5] G. Brezicki, J. Zheng, C. Paolucci, R. Schlögl, R.J. Davis, ACS Catal. 11 (2021) 4973–4987.
[6] M.A. Bañares, Catal. Today 100 (2005) 71–77.
[7] B.M. Weckhuysen, Chem. Commun. (2002) 97–110.
[8] B.M. Weckhuysen, Phys. Chem. Chem. Phys. 5 (2003) 4351–4360.
[9] S.J. Tinnemans, J.G. Mesu, K. Kervinen, T. Visser, T.A. Nijhuis, A.M. Beale, D. E. Keller, A.M.J. van der Eerden, B.M. Weckhuysen, Catal. Today 113 (2006) 3–15.
[10] P.J. Smeets, J.S. Woertink, B.F. Sels, E.I. Solomon, R.A. Schoonheydt, Inorg. Chem. 49 (2010) 3573–3583.
[11] M.A. Newton, A.J. Knorpp, V.L. Sushkevich, D. Palagin, J.A. van Bokhoven, Chem. Soc. Rev. 49 (2020) 1449–1486.
[12] P. Vanelderen, J. Vancauwenbergh, M.-L. Tsai, R.G. Hadt, E.I. Solomon, R. A. Schoonheydt, B.F. Sels, ChemPhysChem 15 (2014) 91–99.
[13] R.A. Schoonheydt, Chem. Soc. Rev. 39 (2010) 5051–5066.
[14] J. Dedecek, Z. Sobalik, Z. Tvaruazkova, D. Kaucky, B. Wichterlova, J. Phys. Chem. 99 (1995) 16327–16337.
[15] A. Godiksen, P.N.R. Vennestrøm, S.B. Rasmussen, S. Mossin, Top. Catal. 60 (2017) 13–29.
[16] M.H. Groothaert, K. Pierloot, A. Delabie, R.A. Schoonheydt, Phys. Chem. Chem. Phys. 5 (2003) 2135–2144.
[17] A. Godiksen, F.N. Stappen, P.N.R. Vennestrøm, F. Giordanino, S.B. Rasmussen, L. F. Lundegaard, S. Mossin, J. Phys. Chem. C. 118 (2014) 23126–23138.
[18] V.L. Sushkevich, D. Palagin, J.A. van Bokhoven, Angew. Chem. Int. Ed. 57 (2018) 8906–8910.
[19] S. Grundner, M.A.C. Markovits, G. Li, M. Tromp, E.A. Pidko, E.J.M. Hensen, A. Jentys, M. Sanchez-Sanchez, J.A. Lercher, Nat. Commun. 6 (2015) 7546.
[20] J.S. Woertink, P.J. Smeets, M.H. Groothaert, M.A. Vance, B.F. Sels, R. A. Schoonheydt, E.I. Solomon, Proc. Natl. Acad. Sci. USA 106 (2009) 18908–18913.
[21] M.H. Groothaert, P.J. Smeets, B.F. Sels, P.A. Jacobs, R.A. Schoonheydt, J. Am. Chem. Soc. 127 (2005) 1394–1395.
[22] M.A. Artsiusheuski, J.A. van Bokhoven, V.L. Sushkevich, ACS Catal. 12 (2022) 15626–15637.
[23] V.L. Sushkevich, M. Artsiusheuski, D. Klose, G. Jeschke, J.A. van Bokhoven, Angew. Chem. Int. Ed. 60 (2021) 15944–15953.
[24] J.W.A. Fischer, A. Brenig, D. Klose, J.A. van Bokhoven, V.L. Sushkevich, G. Jeschke, Angew. Chem. Int. Ed. 62 (2023) e202303574.
[25] F.C. Jentoft, Adv. Catal, 52, Academic Press, 2009, pp. 129–211.
[26] F.M. Mirabella, Modern Techniques in Applied Molecular Spectroscopy, John Wiley & Sons, 1998.
[27] R. Czoch, Appl. Magn. Reson. 10 (1996) 293–317.
[28] A.V. Kucherov, H.G. Karge, R. Schlögl, Microporous Mesoporous Mater. 25 (1998) 7–14.
[29] S.C. Larsen, A. Aylor, A.T. Bell, J.A. Reimer, J. Phys. Chem. U.S. 98 (1994) 11533–11540.
[30] P.C. Bruzzese, E. Salvadori, B. Civalleri, S. Jäger, M. Hartmann, A. Pöppl, M. Chiesa, J. Am. Chem. Soc. 144 (2022) 13079–13083.
[31] B.M. Weckhuysen, D. Baetens, R.A. Schoonheydt, Angew. Chem. Int. Ed. 39 (2000) 3419–3422.
[32] A. Brückner, Chem. Commun. (2001) 2122–2123.
[33] A. Brückner, Chem. Commun. (2005) 1761–1763.
[34] H. Topsøe, J. Catal. 216 (2003) 155–164.
[35] D. Ferri, M.A. Newton, M. Nachtegaal, Top. Catal. 54 (2011) 1070.
[36] B.M. Weckhuysen, Phys. Chem. Chem. Phys. 5 (2003), 4351-4360.
[37] A. Urakawa, T. Bürgi, A. Baiker, Chem. Eng. Sci. 63 (2008) 4902–4909.
[38] T.A. (Xander) Nijhuis, S.J. Tinnemans, T. Visser, B.M. Weckhuysen, Phys. Chem. Chem. Phys. 5 (2003) 4361–4365.
[39] F. Buttignol, D. Rentsch, I. Alxneit, A. Garbujo, P. Biasi, O. Kröcher, D. Ferri, Catal. Sci. Technol. 12 (2022) 7308–7321.

[40] G. Zichittella, Y. Polyhach, R. Tschaggelar, G. Jeschke, J. Pérez-Ramírez, Angew. Chem. 133 (2021) 3640–3646.
[41] O. Müller, M. Nachtegaal, J. Just, D. Lützenkirchen-Hecht, R. Frahm, J. Synchrotron Radiat. 23 (2016) 260–266.
[42] A. Boubnov, H.W.P. Carvalho, D.E. Doronkin, T. Günter, E. Gallo, A.J. Atkins, C. R. Jacob, J.-D. Grunwaldt, J. Am. Chem. Soc. 136 (2014) 13006–13015.
[43] M.A. Newton, A.J. Knorpp, J. Meyet, D. Stoian, M. Nachtegaal, A.H. Clark, O. V. Safonova, H. Emerich, W. van Beek, V.L. Sushkevich, J.A. van Bokhoven, Phys. Chem. Chem. Phys. 22 (2020) 6826–6837.
[44] A.H. Clark, P. Steiger, B. Bornmann, S. Hitz, R. Frahm, D. Ferri, M. Nachtegaal, J. Synchrotron Radiat. 27 (2020) 681–688.
[45] G.L. Chiarello, M. Nachtegaal, V. Marchionni, L. Quaroni, D. Ferri, Rev. Sci. Instrum. 85 (2014) 074102.
[46] A.H. Clark, J. Imbao, R. Frahm, M. Nachtegaal, J. Synchrotron Radiat. 27 (2020) 551–557.
[47] D.T. Bregante, L.N. Wilcox, C. Liu, C. Paolucci, R. Gounder, D.W. Flaherty, ACS Catal. 11 (2021) 11873–11884.
[48] A. Delabie, K. Pierloot, M.H. Groothaert, B.M. Weckhuysen, R.A. Schoonheydt, Phys. Chem. Chem. Phys. 4 (2002) 134–145.
[49] P. Vanelderen, J. Vancauwenbergh, B.F. Sels, R.A. Schoonheydt, Coord. Chem. Rev. 257 (2013) 483–494.
[50] J. Dedecek, Z. Sobalik, Z. Tvaruazkova, D. Kaucky, B. Wichterlova, J. Phys. Chem. 99 (1995) 16327–16337.
[51] A.J. Heyer, D. Plessers, A. Braun, H.M. Rhoda, M.L. Bols, B. Hedman, K. O. Hodgson, R.A. Schoonheydt, B.F. Sels, E.I. Solomon, J. Am. Chem. Soc. 144 (2022) 19305–19316.
[52] M.H. Mahyuddin, E.T. Lasiman, A.G. Saputro, S.V. Casuarina, Nugraha, H.K. Dipojono, Catal. Sci. Technol. 13 (2023) 5767-5775.
[53] S. Yasumura, Y. Qian, T. Kato, S. Mine, T. Toyao, Z. Maeno, K. Shimizu, ACS Catal. 12 (2022) 9983–9993.
[54] R.P. Vélez, U. Bentrup, W. Grünert, A. Brückner, Top. Catal. 60 (2017) 1641–1652.
[55] M. Xiao, J. Zhu, L. Ma, Z. Jin, J. Ge, X. Deng, Y. Hou, Q. He, J. Li, Q. Jia, S. Mukerjee, R. Yang, Z. Jiang, D. Su, C. Liu, W. Xing, ACS Catal. 8 (2018) 2824–2832.
[56] K. Ebner, A.H. Clark, V.A. Saveleva, G. Smolentsev, J. Chen, L. Ni, J. Li, A. Zitolo, F. Jaouen, U.I. Kramm, T.J. Schmidt, J. Herranz, Adv. Energy Mater. 12 (2022) 2103699.
[57] J. Pérez-Ramírez, M. Santhosh Kumar, A. Brückner, J. Catal. 223 (2004) 13–27.
[58] S. Hansen, W. Müller-Warmuth, Ber. Bunsenges. Für Phys. Chem. 95 (1991), 1307–1307.
[59] E. Berrier, O. Ovsitser, E.V. Kondratenko, M. Schwidder, W. Grünert, A. Brückner, J. Catal. 249 (2007) 67–78.
[60] A.V. Kucherov, C.N. Montreuil, T.N. Kucherova, M. Shelef, Catal. Lett. 56 (1998) 173–181.
[61] A.V. Kucherov, A.A. Slinkin, Zeolites 8 (1988) 110–116.
[62] V.L. Sushkevich, O.V. Safonova, D. Palagin, M.A. Newton, J.A. van Bokhoven, Chem. Sci. 11 (2020) 5299–5312.
[63] I. Ellmers, R. Pérez Vélez, U. Bentrup, W. Schwieger, A. Brückner, W. Grünert, Catal. Today 258 (2015) 337–346.
[64] M. Høj, M.J. Beier, J.-D. Grunwaldt, S. Dahl, Appl. Catal. B Environ. 93 (2009) 166–176.